ENDORSED BY

IPEM Institute of Physics and
Engineering in Medicine

PAPER

Water-dispersible magnetite nanoparticles as T_2 MR imaging contrast agent

View the article online for updates and enhancements.

Related content

Recent citations

Biomedical Physics & Engineering Express

PAPER

Water-dispersible magnetite nanoparticles as T_2 MR imaging contrast agent

M Ravichandran[1]**, S Velumani**[1,2] **and Jose Tapia Ramirez**[3]

[1] Program on Nanoscience and Nanotechnology, CINVESTAV-IPN, Av. 2508 National Polytechnic Institute, Gustavo A. Madero, San Pedro Zacatenco, 07360 Mexico City, Mexico
[2] Department of Electrical Engineering, CINVESTAV-IPN,.Av. 2508 National Polytechnic Institute, Gustavo A. Madero, San Pedro Zacatenco, 07360 Mexico City, Mexico
[3] Department of Genetics and Molecular Biology, CINVESTAV-IPN, Av. 2508 National Polytechnic Institute, Gustavo A. Madero, San Pedro Zacatenco, 07360 Mexico City, Mexico

E-mail: velu@cinvestav.mx

Keywords: magnetite, CTAB, water-dispersible, superparamagnetic, contrast agent

Supplementary material for this article is available online

Abstract

Water-dispersible iron oxide nanoparticles (NPs) consistently demonstrated a significant interest in the field of biomedical applications. Through this report, we present the synthesis of monodispersed magnetite NPs with an excellent water-dispersibility by employing a modified thermal decomposition method. Synthesized NPs were characterized by x-ray diffraction, transmission electron microscopy, x-ray photoelectron spectroscopy, vibrating sample magnetometry and cytotoxicity assay. From the results, it is evident that the NPs are highly crystalline, of spherical morphology with diameters of 20 ± 1 nm, superparamagnetic, and cytocompatible. Finally, we probed NPs as a T_2-weighted contrast agent in magnetic resonance Imaging which resulted in relatively high r_2 values. Therefore, the NPs could be effectively used as a potential candidate for various biological applications.

1. Introduction

In the past two decades, magnetic nanoparticles (NPs) showed considerable importance in the medical applications [1] because of its interesting physico-chemical properties [2]. Among these NPs, magnetite NPs (MNPs) are widely employed for various biological applications such as drug delivery, hyperthermia, and magnetic resonance imaging (MRI) [3, 4]. However, to effectively use MNPs in said applications, the important criteria are that the NPs must be water-dispersible [5], monodispersed with narrow particle size, high crystallinity, biocompatible, and so forth [2]. Thus, the researchers tend to use reactants that are expensive and toxic, such as surfactants and solvents [6]. Therefore, it is always remained as a great challenge to design a simple method for synthesizing highly water-dispersible MNPs.

There are very few reports available on the synthesis of water-dispersible MNPs by thermal decomposition (TD) method. In general, this technique involves using multiple reactants such as triethylene glycol [5], diethylene glycol [7], 1,2-hexadecanediol

[8], 1,2-dodecanediol [9], oleic acid, octyl ether, oleylamine, phenyl ether, hexadecane, eicosene, and dioctyl ether [10]. Furthermore, the above protocol requires a ligand-exchange process to make the NPs as hydrophilic, essentially using surfactants such as polyethylene glycol [11], pluronic F127, [12] silica [13], and cetyltrimethylammonium bromide (CTAB) [14–22].

In our case, we have combined the above procedures into a one-pot technique to directly synthesize water-dispersible MNPs without the necessity of ligand-exchange process. The synthesis involves using benzyl ether as a solvent assisting in reducing the metal precursor, and CTAB, the widely used cationic surfactant, to provide a surface charge to prevent the NPs from being agglomerated. However, the major disadvantage of CTAB is its toxicity. Nevertheless, this could be completely minimized by using it appropriately [23]. In this report, we have discussed the synthesis and characterization of water-dispersible CTA^+ stabilized magnetite nanoparticles (C-MNPs) and investigated the cell viability by MTT [3-(4,5-dimethylthiazol-2-yl)-2,5-diphenyltetrazolium

bromide] assay [24], as well as the possibilities of using them as a potential T_2 contrast agent.

2. Materials and methods

2.1. Materials
All the chemical reagents were purchased from Sigma-Aldrich, Mexico and used without further purification, unless or otherwise stated; iron (III) acetylacetonate (Fe(acac)$_3$, Fe(C$_5$H$_7$O$_2$)$_3$, $\geqslant$99.9%), hexadecyltrimethylammonium bromide (CTAB, CH$_3$(CH$_2$)$_{15}$N(Br)(CH$_3$)$_3$, $\geqslant$99%), benzyl ether (BE, (C$_6$H$_5$CH$_2$)$_2$O, $\geqslant$98%), dimethyl sulfoxide (DMSO, (CH$_3$)$_2$SO, $\geqslant$99.9%), ethanol (EtOH, CH$_3$CH$_2$OH, $\geqslant$99.8%), and MTT (C$_{18}$H$_{17}$N$_5$S, $\geqslant$97%). Cell culture reagents like Dulbecco's Modified Eagle Medium (DMEM), fetal bovine serum, and streptomycin were purchased from Gibco, Thermo Fisher Scientific Inc.

2.2. Synthesis of CTAB stabilized magnetite nanoparticles (C-MNPs)
C-MNPs were synthesized by employing modified protocol of TD technique. Initially, 2 mmol of Fe(acac)$_3$ was dissolved in 20 ml of BE in a three-neck round-bottom flask; to this is added CTAB with various molar concentrations (0.1, 0.2, and 0.3 M). The reaction was carried out with the aid of heating mantle to provide uniform heating throughout the flask. The refluxing was carried out at 260 °C, under continuous and vigorous stirring in a nitrogen atmosphere (N$_2$ atm) for one hour, and was naturally cool down to room temperature. Subsequently, 150 ml of EtOH was added to precipitate the C-MNPs. Later, the solution was centrifuged (at 4000 rpm, for 15 min) to remove excess CTAB. The black pellet-like residue was collected and washed with EtOH. The resultant material was dispersed in de-ionized water and was stored until further use.

2.3. Characterization techniques
The structure and crystallinity of the C-MNPs were probed by PAN analytical, X'Pert Powder x-ray diffractometer (XRD) using Cu-Kα radiation ($\lambda = 0.154$ nm) with 2θ angles ranging from 10° to 90° at a scan rate of 0.02/1 s. The sample was prepared by drop-casting few drops of C-MNP solution onto the glass substrate. The morphology and size of C-MNPs were analyzed using both Low (TEM, Jeol JEM-2100) and high-resolution transmission electron microscopy (Jeol ARM200F). The TEM sample grid was prepared by placing a drop of water-dispersed C-MNPs onto the carbon film 300 mesh copper grid (Ted Pella, Inc.), and was dried in a vacuum desiccator over anhydrous calcium sulfate for 24 h prior to the analysis. The NP hydrodynamic size was measured using dynamic light scattering (DLS) technique by employing Zetasizer Nano ZS90 (Malvern Instruments) on C-MNPs samples in deionized water at a

wavelength of 633 nm at 25 °C. Thermogravimetric analysis was carried out using a TGA Q50 (TA Instruments) from 30 °C to 600 °C at a heating rate of 10 °C min^{-1} in a N$_2$ atm to study the % weight loss of NPs. Further to evaluate the magnetization and magnetic behavior, magnetic hysteresis loops were recorded for a known amount of NPs in the sample holder under the applied field of -7500 to 7500 Oe by using Vibrating Sample Magnetometry (VSM, Quantum Design, PPMS DynaCool). X-ray photoelectron spectroscopy (XPS) analysis was conducted to identify the elemental composition and their oxidation states using a K-Alpha XPS System (Surface Analysis, Thermo Scientific) equipped with monochromated Al-Kα x-ray source. The XPS data were calibrated using the binding energy of C1s.
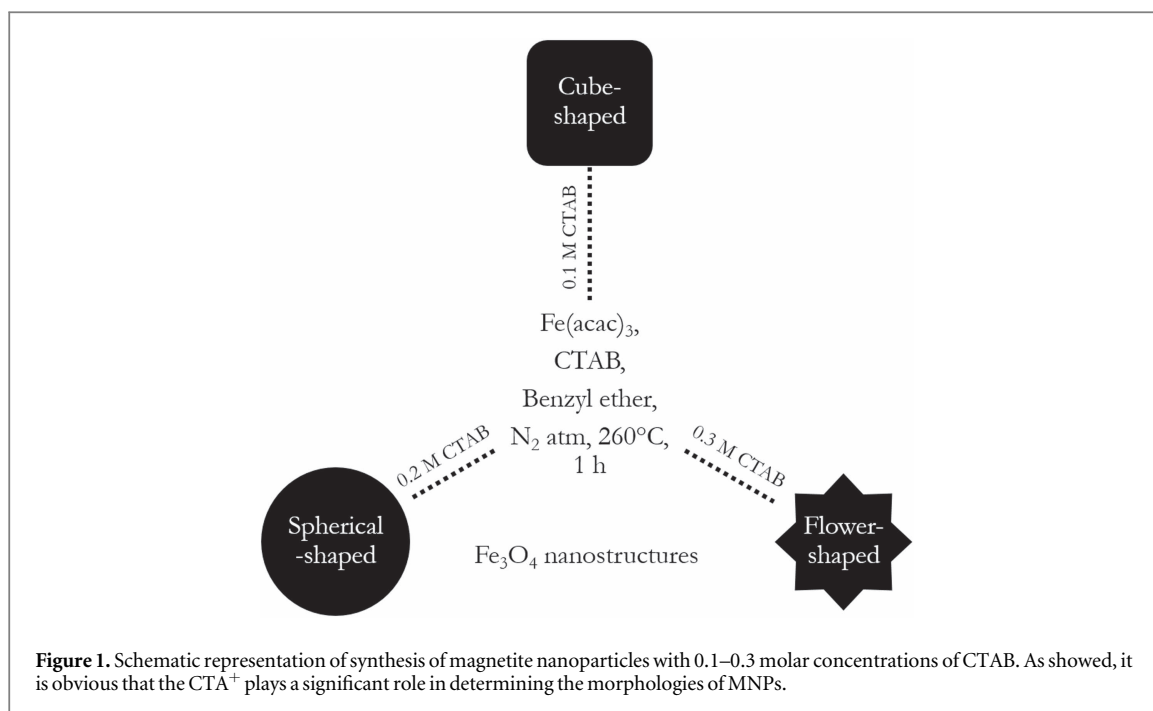
2.4. MRI analysis
MRI experiments were performed on a 7 T scanner (Clinical Signa HDxt scanner Varian). Known concentrations of C-MNPs were dispersed in 2 ml of water in an Eppendorf tube. T_2-weighted images were obtained using the following parameters; repetition time (TR) = 2000 ms, echo time (TE) = 15 ms, with a resolution of 256 × 256 points, and a slice thickness of 4 mm at room temperature. For T_1 measurements, spin-echo sequences with a constant TE of 24 ms and varying TR from 50 ms to 5 s were used.

2.5. Cell viability assay
Cell viability studies were performed using MTT assay as given below:

- Both L6 (skeletal muscle cell line) and Hep2 cells (laryngeal carcinoma cell line) were cultured in DMEM supplemented with 10% fetal bovine serum and 100 μg ml^{-1} streptomycin in an incubator with 5% CO$_2$ atmosphere at 37 °C.

- Cells were seeded into a 12-well plate at a cell density of 1 × 10^5 cells/plate.

- Subsequently, various concentrations (50 $-$250 μg ml^{-1}) of C-MNPs were added.

- Then, a 10 μl of MTT (5 mg ml^{-1}) in DMEM was added and incubated for 3 h.

- After incubation, excess MTT solution was removed, and a 200 μl of DMSO was added to dissolve the formazan crystals.

- The plates were kept on a shaker for 10 min followed by 24 h incubation.

- Later, absorbance was recorded at 570 nm using an iMark microplate reader (Bio-Rad Laboratories).

The measurements were recorded in triplicates and viability data was obtained from their average values.

Figure 1. Schematic representation of synthesis of magnetite nanoparticles with 0.1–0.3 molar concentrations of CTAB. As showed, it is obvious that the CTA^+ plays a significant role in determining the morphologies of MNPs.

3. Results and discussions

The main aim of this synthesis was to produce highly monodispersed, readily water-dispersable, and importantly biocompatible MNPs using CTAB. It is well-known that CTAB is employed to synthesize various metal NPs with precise morphologies [25–27] resulting in smaller and uniform NPs [28] by specific interaction with lattice planes [29]. The growth of an NP is determined by two factors that affect the crystal facets [30, 31], viz.,
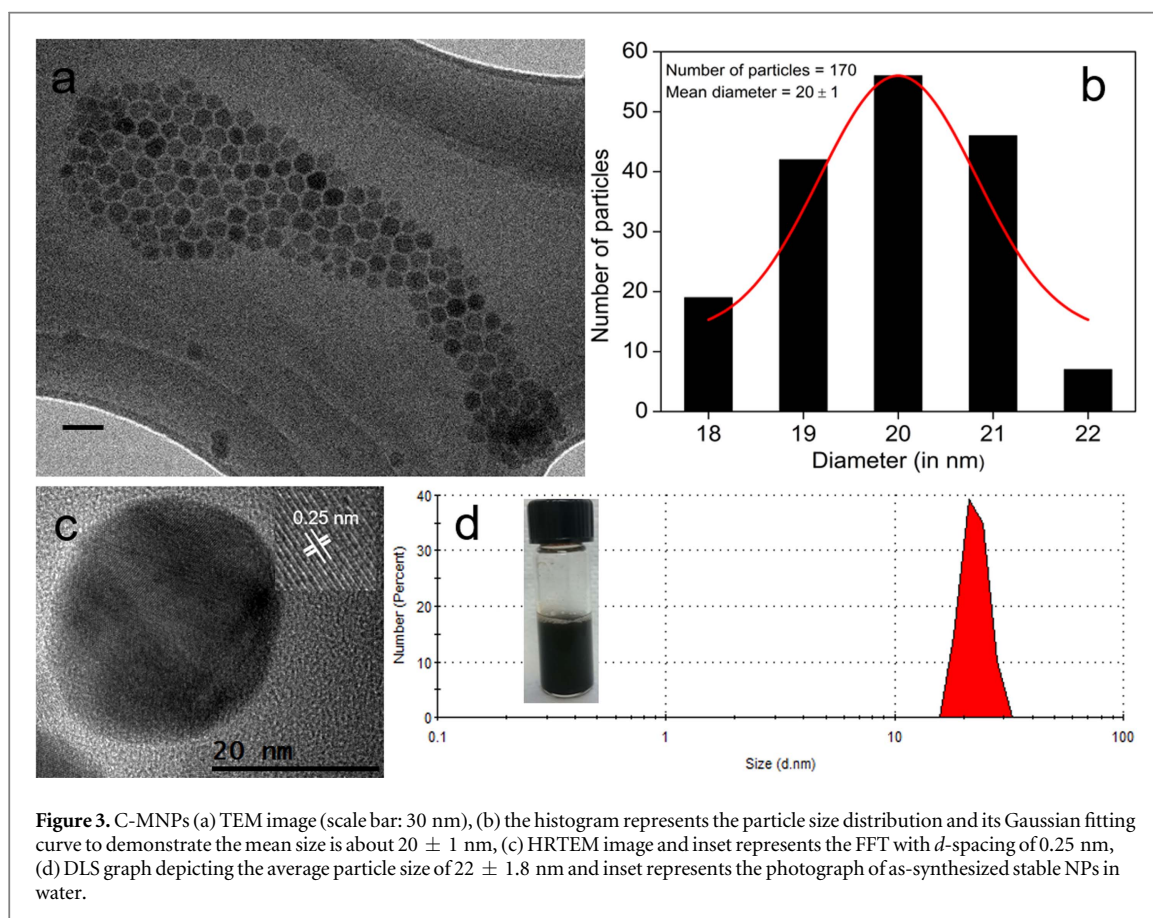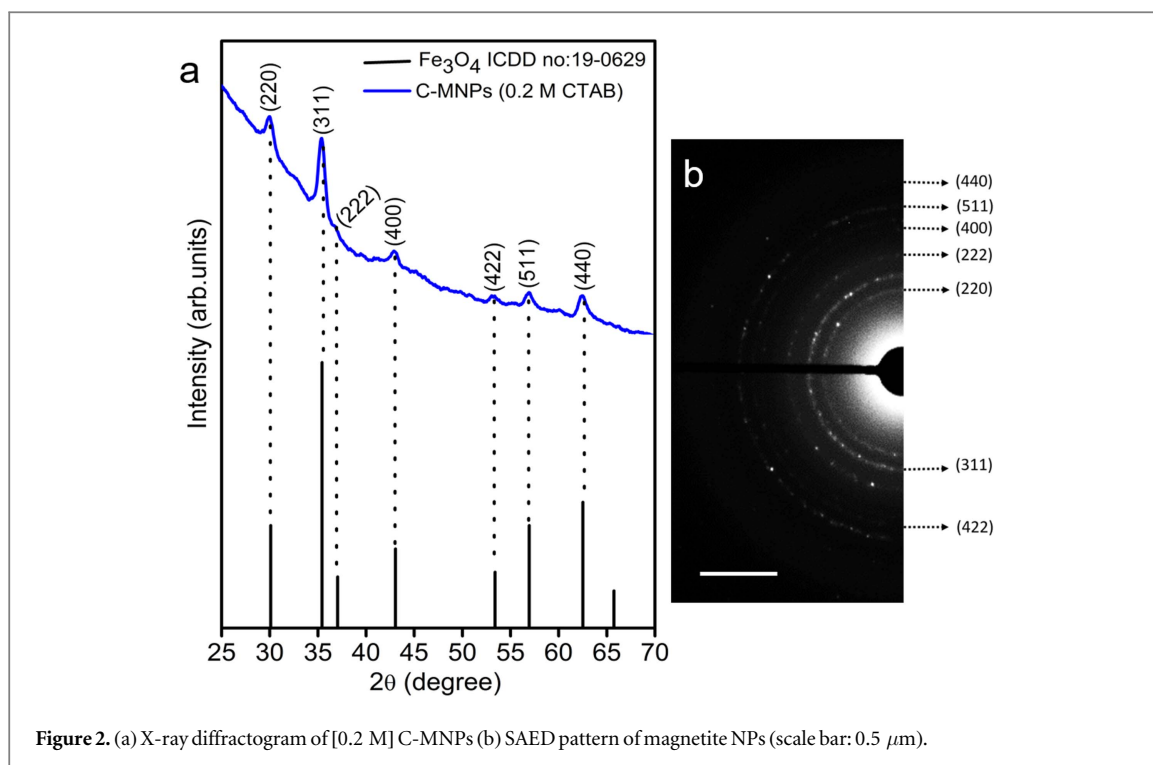
- Thermodynamically controlled: uniform growth (spherical structures), e.g., spherical NPs

- Kinetically controlled: preferential/directional growth (anisotropic structures), e.g., rods, cubes, prisms.

Usually, the morphology of an NP is affected during the process of crystallization by the selective binding of surfactant moieties in the various positions of the crystal [32–34]. Therefore, considering the function of the surfactant; the as-synthesized NPs (spherical-morphology) was probed by several characterization techniques to study in-depth properties and to evaluate their possibility as a T_2 contrast agent. Figure 1 depicts the facile method that we adapted for the synthesis of C-MNPs.

XRD pattern, as shown in figure 2(a), reveals the crystallinity of C-MNPs synthesized with 0.2 M CTAB. All peaks are well indexed to face-centered cubic Fe_3O_4 lattice and are in corroboration with the International Centre for Diffraction Data reference pattern, no:19-0629. It is apparent from the pattern that there is no sign of secondary phase formation

which is clearly due to the maintenance of N_2 atm throughout the reaction. The noisy and amorphous background in the pattern corresponds to the amorphous glass substrate [35]. The average crystallite size has been calculated using Scherrer formula [36], considering the spherical shape of the NPs, as 16.4 nm, and is in corroboration with TEM analysis. The diffraction rings from the selected area electron diffraction pattern corresponds to the MNPs, as represented in the inset of figure 2(b), which also confirms the crystallinity of the NPs [5].

Figure 3(a) shows the transmission electron (TE) micrographs revealing the formation of spherical morphologies of C-MNPs synthesized with 0.2 molar concentrations of CTAB. The distorted cubical, and flower-like morphologies of C-MNPs synthesized with 0.1, and 0.3 molar CTAB concentrations, respectively are shown in figures S1(a) and (b) in the ESI. It is apparent that the addition of CTAB has clearly affected the NPs formation by producing a series of morphologies with precise growth in the 'nm' range. Sayed *et al* reported the formation of similar nanostructures when CTAB was employed in the synthesis of maghemite NPs [37]. The possible formation mechanism of the various morphologies is as explained below: in case of cube, the morphology is minorly distorted and the edges were indistinct. It is due to the insufficient reaction time [38], even though the CTA^+ ions initiated the directional growth by anchoring to Fe_3O_4 surface [39]. Therefore, the synthesis time have to be prolonged to obtain monodisperse cube shaped NPs. The spherical shape formation is mostly energy based during the NPs growth process. Due to high concentration of surfactant moieties onto the surface of metal seeds, it leads to less surface energy on NPs. Therefore, as the surface energy of spherical NPs is very low when

Figure 2. (a) X-ray diffractogram of [0.2 M] C-MNPs (b) SAED pattern of magnetite NPs (scale bar: 0.5 μm).

Figure 3. C-MNPs (a) TEM image (scale bar: 30 nm), (b) the histogram represents the particle size distribution and its Gaussian fitting curve to demonstrate the mean size is about 20 ± 1 nm, (c) HRTEM image and inset represents the FFT with *d*-spacing of 0.25 nm, (d) DLS graph depicting the average particle size of 22 ± 1.8 nm and inset represents the photograph of as-synthesized stable NPs in water.

compared to other anisotropic NPs, the possibility is comparatively higher to form spherical shaped NPs [40]. The flower-shaped NPs is due to the self-assembly/clustering of individual NPs which assemble from the centre to form a multicore flower structure [41].

Therefore, from the above interpretation, it is evident that CTAB plays a dual role as both coating and shape-directing agent [42].

In this report, we have concentrated only on the synthesis and characterization of spherical NPs as it is
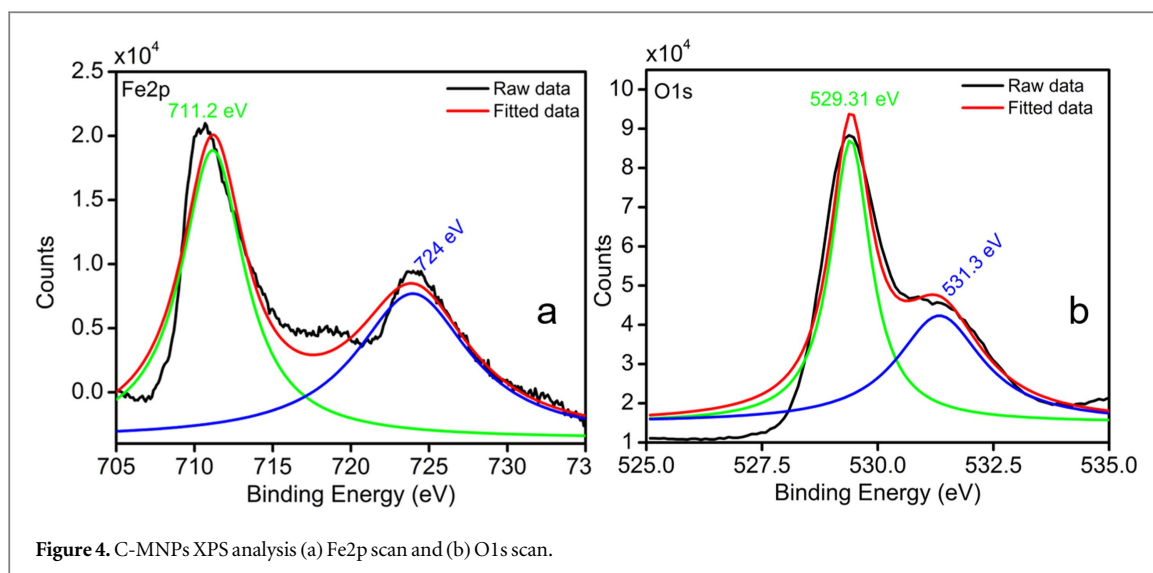
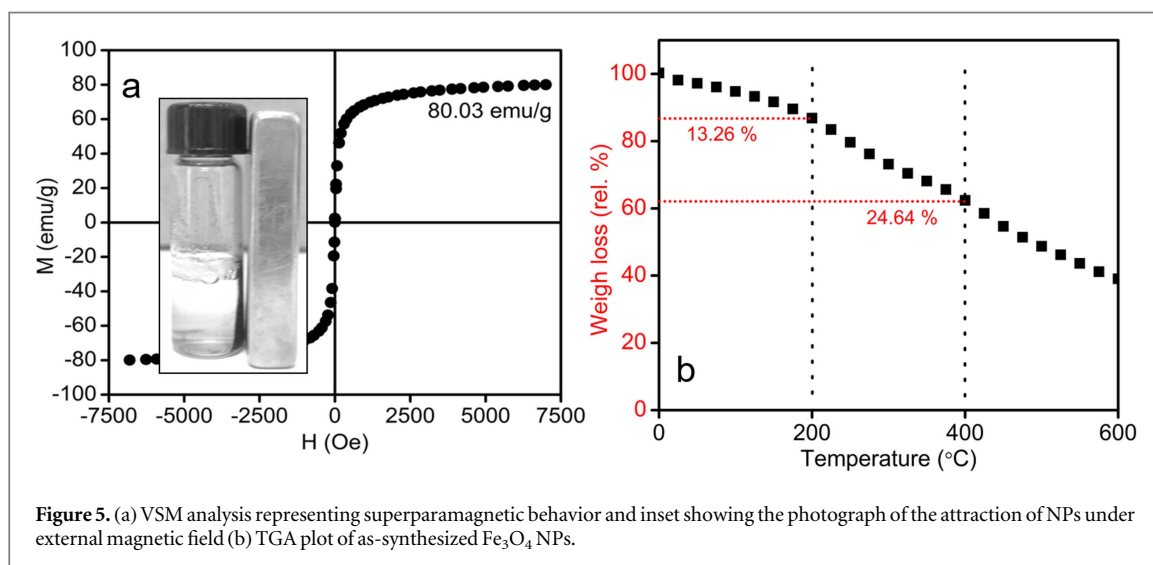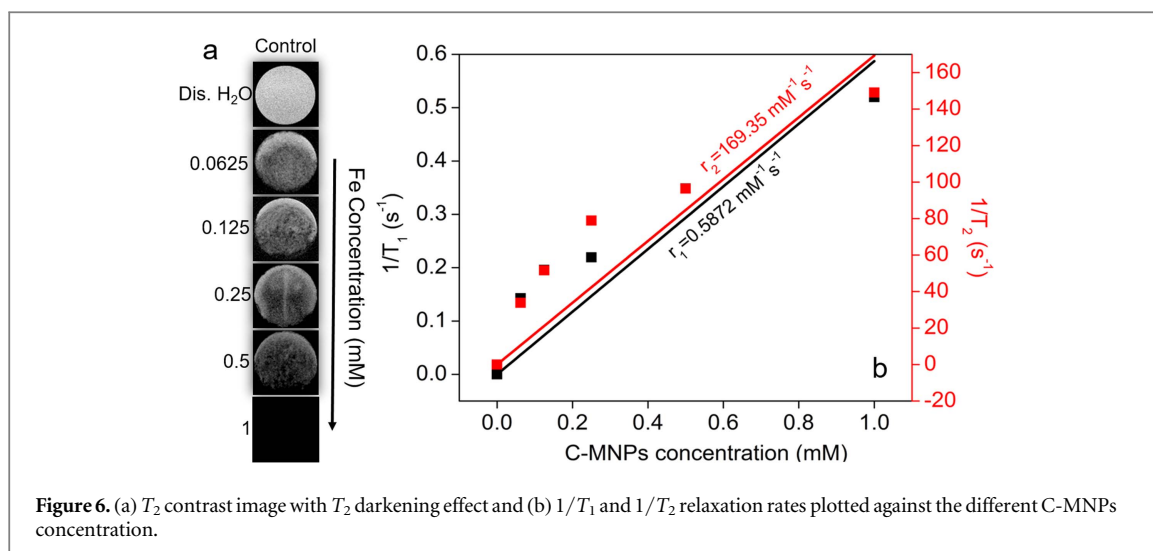**Figure 4.** C-MNPs XPS analysis (a) Fe2p scan and (b) O1s scan.

Figure 5. (a) VSM analysis representing superparamagnetic behavior and inset showing the photograph of the attraction of NPs under external magnetic field (b) TGA plot of as-synthesized Fe_3O_4 NPs.

widely employed for biological applications [43], whereas further investigations are needed for distorted cubical and flower-like nanomaterials. TE micrograph in figure 3(a) shows the spherical morphology of the C-MNPs exhibiting monodispersity, and non-aggregation. The reason behind the non-aggregation is due to the electrostatic repulsion among the head groups of CTA^+ on the neighboring NPs. We manually measured the size of 170 NPs, using Gatan software (Digital Micrograph 3.7.0), and the distribution is as depicted in the histogram (figure 3(b)). The average size is thus calculated to be 20 ± 1 nm. Figure 3(c) shows the HRTE micrograph of C-MNPs revealing it to be a single crystal [9], and corresponding inset depicts the fast Fourier transformation (FFT) image. The interplanar distance is measured, from FFT, to be 0.25 nm which corresponds to the (311) plane of the magnetite structure.

DLS analysis was performed on shelf stored water-dispersed C-MNPs to determine the particle's hydrodynamic size which plays a crucial factor for *in vivo* applications [44, 45]. The average hydrodynamic size

of NPs is found to be 22 ± 1.8 nm (figure 3(d)), and the apparent increase in the relative size to TEM measurements is due to the adsorbing layer of CTA^+ onto the NPs surface [5]. Inset in the figure 3(f) shows the photograph of the vial containing the colloidal C-MNPs in water.

The CTA^+'s adsorption on the NPs surface were investigated using XPS. The data (figures 4(a) and (b)) represents the core level spectra of Fe2p and O1s scans. Usually, MNPs exhibit two strong peaks at binding energies of 709 and 722.9 eV for Fe 2p3/2 and Fe 2p1/2 respectively [46]. However, in our case, Fe2p scan shows two strong peaks at 711.2 and 724 eV corresponding to Fe2p3/2 and Fe2p1/2 respectively with a minor shift in the binding energy values indicating the efficient adsorption of CTA^+ onto the NP's surface. Moreover, the experimental data shows no peak at 719.0 eV, which additionally supports that the synthesized product is pure magnetite rather than maghemite. Furthermore, the O1s scan exhibited two strong peaks (529.31 and 531.3 eV) corresponding to the Fe–O bonding in magnetite [5, 47].

Figure 6. (a) T_2 contrast image with T_2 darkening effect and (b) $1/T_1$ and $1/T_2$ relaxation rates plotted against the different C-MNPs concentration.

Magnetic measurements (figure 5(a)) revealed the superparamagnetic behavior of the NPs at room temperature with the magnetization value (Ms) of 80.03 emu g^{-1} and a little remanence (Mr) of ca. 2.69 emu g^{-1}. Magnetic NPs lesser than 20 nm exhibits superparamagnetic behavior with negligible remanence [48] which can strongly enhance the proton relaxation resulting to high r_2 values [49, 50]. The remanence to saturation ratio ($R = Mr/Ms$) was found to be 0.033. Nonetheless, the remanence ratio (Mr/Ms) is lower than that expected for a ferromagnet (Mr/Ms = 0.8) suggesting the source of anisotropy which is intrinsic magnetocrystalline anisotropy. However, this Ms value is comparatively higher than that of other MNPs, synthesized via TD method [7, 10] which could be attributed to the crystallinity of C-MNPs [51] due to its substantial impact on the Ms [52].

TGA measurements (figure 5(b)) depict that the NPs are stable even at higher temperatures. The initial weight loss of 13.26% up to 200 °C signifies the evaporation of water molecules from the surface of NPs. The second weight loss (24.64%) from 200 °C to 400 °C may be attributed to the complete decomposition of organic CTAB moieties [53]. However, the weight loss from 400 °C continues further which indicates the transformation of MNPs, to maghemite and may finally lead to hematite [54].

We effectively employed C-MNPs as a contrast agent in MR imaging using the 7 T scanner to investigate its property further. MR imaging is one of the finest tools used for non-invasive clinical diagnosis, due to its significant advantages such as high penetration depth and soft tissue contrast, to obtain images safely without any side-effects [55]. This technique distinguishes and improves the image quality of unhealthy lesions using contrast agents [56]. Figure 6(a) shows the T_2 signal from the water-dispersed C-MNPs of different concentrations. It is observed that the signal intensity increases with the NPs concentration as seen from the darkening effect. Therefore, this contrast enhancement is due to the exceptional properties of C-MNPs, such as size, shape, magnetic behavior, and so forth [57]. We have measured both transverse and longitudinal relaxivities. From which it is corroborated that these NPs express T_2 imaging effect (r_2 value = 169.35 mM^{-1} s^{-1}) rather than T_1 (r_1 value = 0.5872 mM^{-1} s^{-1}) by calculating the r_2/r_1 ratio which is found to be 288.4. Figure 6(b) represents the relaxation rates $1/T_1$ and $1/T_2$ as a function of the NPs concentration. The r_2 value is higher than the commercially available products. Such as, Ferumoxides (Feridex) r_2 value of 132 mM^{-1} s^{-1} at 7 T [58]. Moreover, also the r_2 values (7 T) was 10-fold higher than that of CTAB stabilized MNPs which was 15.4 mM^{-1} s^{-1} [20].

From the above studies, it is very clear that the synthesized C-MNPs satisfies to be a high-performance MR imaging probe [59] by fulfilling the following characteristics, such as,

- High saturation magnetization because of its high crystallinity,

- monodispersed NPs which can extend the circulation time in the blood pool,

- highly water-dispersible and biocompatible,

- particle size is less than 200 nm so it can easily be cleared by human spleen [60],

- proven to be relatively a better T_2 contrast agent with high r_2/r_1 ratio [12].

To evaluate the C-MNPs cytotoxic effects, we employed MTT assay to detect cell viability using normal L6 and cancerous Hep2 cells (figure 7). It is clearly observed that the presence of NPs in the medium does not affect the cells even at higher concentrations of 250 μg ml^{-1}. Therefore, we can conclude that the NPs are highly cytocompatible by CTAB coating rather
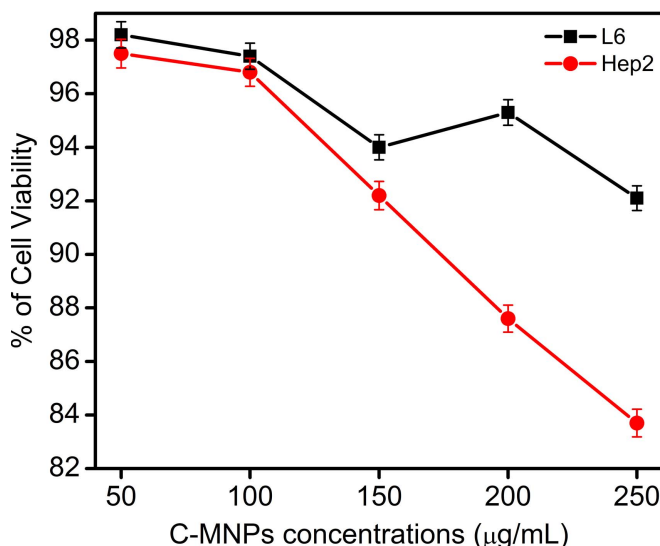
Figure 7. Cytotoxicity study of C-MNPs concentration using MTT assay with L6 and Hep2 cells.

than the naked NPs which usually release toxic ions and affects the biocompatibility [61]. Nevertheless, it is observed that the Hep2 cells exhibited a threshold limit of 80%, which as per our knowledge is due to the inherent capability of the NPs to stimulate apoptosis. Similar behavior was observed with MNPs in HepG2 and A549 cell lines [62].

4. Conclusions

We have demonstrated a simple, and one-pot synthesis method for MNPs using CTAB. Importantly, these NPs are monodispersed and superparamagnetic as observed from TEM analysis and VSM measurements respectively. It is, therefore, evident that the surfactant CTAB has an essential role not only in defining the size of NPs but also acts as a shape determining factor. Additionally, these NPs are water-dispersible that can be readily usable for various biomedical applications without further surface modifications. MTT assay confirms the NPs are cytocompatible. Finally, we have evaluated their huge contrast enhancement in T_2 weighted MR imaging. Therefore, we firmly believe that these MNPs can be used as a potential candidate for contrast imaging agents.

Acknowledgments

References

[1] Lu A H, Salabas E L and Schüth F 2007 Magnetic nanoparticles: Synthesis, protection, functionalization, and application *Angew. Chem., Int. Ed.* **46** 1222–44

[2] Hyeon T 2003 Chemical synthesis of magnetic nanoparticles *Chem. Commun.* **34** 927–34

[3] Pankhurst Q A, Connolly J, Jones S K and Dobson J 2003 Applications of magnetic nanoparticles in biomedicine *J. Phys. D: Appl. Phys.* **36** 167–81

[4] Laurent S, Forge D, Port M, Roch A, Robic C, Vander Elst L and Muller R N 2008 Magnetic iron oxide nanoparticles: synthesis, stabilization, vectorization, physicochemical characterizations and biological applications *Chem. Rev.* **108** 2064–110

[5] Wan J, Cai W, Meng X and Liu E 2007 Monodisperse water-soluble magnetite nanoparticles prepared by polyol process for high-performance magnetic resonance imaging *Chem. Commun.* **4** 5004–6

[6] Wang Z, Zhao L, Yang P, Lv Z, Sun H and Jiang Q 2014 Water-soluble amorphous iron oxide nanoparticles synthesized by a quickly pestling and nontoxic method at room temperature as MRI contrast agents *Chem. Eng. J.* **235** 231–5

[7] Jia X, Chen D, Jiao X and Zhai S 2009 Environmentally-friendly preparation of water-dispersible magnetite nanoparticles *Chem. Commun.* 968–70

[8] Campanini M *et al* 2015 Lorentz microscopy sheds light on the role of dipolar interactions in magnetic hyperthermia *Nanoscale* **7** 7717–25

[9] Yang T, Shen C, Yang H, Xiao C, Xu Z, Chen S, Shi D and Gao H 2006 Synthesis, characterization and self-assemblies of magnetite nanoparticles *Surf. Interface Anal.* **38** 1063–7

[10] Demortière A, Panissod P, Pichon B P, Pourroy G, Guillon D, Donnio B and Bégin-Colin S 2011 Size-dependent properties of magnetic iron oxidenanocrystals *Nanoscale* **3** 225–32

[11] Hu F, Jia Q, Li Y and Gao M 2011 Facile synthesis of ultrasmall PEGylated iron oxide nanoparticles for dual-contrast T_1- and T_2-weighted magnetic resonance imaging *Nanotechnology* **22** 245604

[12] Qin J, Laurent S, Jo Y S, Roch A, Mikhaylova M, Bhujwalla Z M, Müller R N and Muhammed M 2007 A high-performance magnetic resonance imaging T_2 contrast agent *Adv. Mater.* **19** 1874–8

[13] Niu D, Li Y, Zhi M, Diao H, Gu J, Chen H, Zhao W, Ruan M, Zhang Y and Shi J 2010 Preparation of uniform, water-soluble, and multifunctional nanocomposites with tunable sizes *Adv. Funct. Mater.* **20** 773–80

[14] Ye F, Laurent S, Fornara A, Astolfi L, Qin J, Roch A, Martini A, Toprak M S, Muller R N and Muhammed M 2012 Uniform mesoporous silica coated iron oxide nanoparticles as a highly efficient, nontoxic MRI T_2 contrast agent with tunable proton relaxivities *Contrast Media Mol. Imaging* **7** 460–8

[15] Liong M, Lu J, Kovochich M, Xia T, Ruehm S G, Nel A E, Tamanoi F and Zink J I 2008 Multifunctional inorganic nanoparticles for imaging, targeting, and drug delivery *ACS Nano* **2** 889–96

[16] Lee N, Choi Y, Lee Y, Park M, Moon W K, Choi S H and Hyeon T 2012 Water-dispersible ferrimagnetic iron oxide nanocubes with extremely high r_2 relaxivity for highly sensitive *in vivo* MRI of tumors *Nano Lett.* **12** 3127–31

[17] Hu J, Qian Y, Wang X, Liu T and Liu S 2012 Drug-loaded and superparamagnetic iron oxide nanoparticle surface-embedded amphiphilic block copolymer micelles for integrated chemotherapeutic drug delivery and MR imaging *Langmuir* **28** 2073–82

[18] Sanganeria P, Sachar S, Chandra S, Bahadur D, Ray P and Khanna A 2015 Cellular internalization and detailed toxicity analysis of protein-immobilized iron oxide nanoparticles *J. Biomed. Mater. Res.* B **103** 125–34

[19] Kim T *et al* 2011 Mesoporous silica-coated hollow manganese oxide nanoparticles as positive T 1 contrast agents for labeling and MRI tracking of adipose-derived mesenchymal stem cells *J. Am. Chem. Soc.* **133** 2955–61

[20] Qiu P, Jensen C, Charity N, Towner R and Mao C 2010 Oil phase evaporation-induced self-assembly of hydrophobic nanoparticles into spherical clusters with controlled surface chemistry in an oil-in-water dispersion and comparison of behaviors of individual and clustered iron oxide nanoparticles *J. Am. Chem. Soc.* **132** 17724–32

[21] Chen D, Jiang M, Li N, Gu H, Xu Q, Ge J, Xia X and Lu J 2010 Modification of magnetic silica/iron oxide nanocomposites with fluorescent polymethacrylic acid for cancer targeting and drug delivery *J. Mater. Chem.* **20** 6422–9

[22] Guo X, Deng Y, Gu D, Che R and Zhao D 2009 Synthesis and microwave absorption of uniform hematite nanoparticles and their core–shell mesoporous silica nanocomposites *J. Mater. Chem.* **19** 6706

[23] Schachter D 2013 The source of toxicity of CTAB-stabilized gold nanorods *Masters Thesis* 61 The State University of New Jersey and University of Medicine and Dentistry of New Jersey

[24] Riss T L, Niles A L and Minor L 2013 *Cell Viability Assays Assay Guidance Manual* (Bethesda, MD: Eli Lilly)

[25] Murphy C J, Sau T K, Gole A M, Orendorff C J, Gao J, Gou L, Hunyadi S E and Li T 2005 Anisotropic metal nanoparticles: Synthesis, assembly, and optical applications *J. Phys. Chem.* B **109** 13857–70

[26] Cushing B L, Kolesnichenko V L and O'Connor C J 2004 Recent advances in the liquid-phase syntheses of inorganic nanoparticles *Chem. Rev.* **104** 3893–946

[27] Kofke M J, Wierzbinski E and Waldeck D H 2013 Seedless CTAB mediated growth of anisotropic nanoparticles and nanoparticle clusters on nanostructured plasmonic templates *J. Mater. Chem.* C **1** 6774–81

[28] Chen C J, Chiang R K, Wang J S and Wang S L 2013 Synthesis and magnetic properties of octahedral magnetite nanoparticles in 20–110 nm range *J. Nanopart. Res.* **15** 1845

[29] Pu Z, Cao M, Yang J, Huang K and Hu C 2006 Controlled synthesis and growth mechanism of hematite nanorhombohedra, nanorods and nanocubes *Nanotechnology* **17** 799–804

[30] Berhault G, Bausach M, Bisson L, Becerra L, Thomazeau C and Uzio D 2007 Seed-mediated synthesis of Pd nanocrystals: Factors influencing a kinetic- or thermodynamic-controlled growth regime *J. Phys. Chem.* C **111** 5915–25

[31] Sajanlal P R, Sreeprasad T S, Samal A K and Pradeep T 2011 Anisotropic nanomaterials: structure, growth, assembly, and functions *Nano Rev.* **1** 1–62

[32] Aguirre C M, Kaspar T R, Radloff C and Halas N J 2003 CTAB mediated reshaping of metallodielectric nanoparticles *Nano Lett.* **3** 1707–11

[33] Sun Y, Mayers B, Herricks T and Xia Y 2003 Polyol synthesis of uniform silver nanowires: a plausible growth mechanism and the supporting evidence *Nano Lett.* **3** 955–60

[34] Johnson C J, Dujardin E, Davis S A, Murphy C J and Mann S 2002 Growth and form of gold nanorods prepared by seed-mediated, surfactant-directed synthesis *J. Mater. Chem.* **12** 1765–70

[35] Ambekar J D, Panmand R P, Sonawane R S, Apte S K, Hundiwale D G and Kale B B 2015 Preparation and magneto-optical properties of stable bismuth phosphate nanoparticles in phosphate glass *RSC Adv.* **5** 48112–7

[36] Patterson A L 1939 The scherrer formula for x-ray partcile size determination *Phys. Rev.* **56** 978–82

[37] Sayed F N and Polshettiwar V 2015 Facile and sustainable synthesis of shaped iron oxide nanoparticles: effect of iron precursor salts on the shapes of iron oxides *Sci. Rep.* **5** 9733

[38] Bakshi M S 2016 How surfactants control crystal growth of nanomaterials *Cryst. Growth Des.* **16** 1104–33

[39] Thomas K G, Barazzouk S, Ipe B I, Joseph S T S and Kamat P V 2004 Uniaxial plasmon coupling through longitudinal self-assembly of gold nanorods *J. Phys. Chem.* B **108** 13066–8

[40] Fu Y, Du Y, Yang P, Li J and Jiang L 2007 Shape-controlled synthesis of highly monodisperse and small size gold nanoparticles *Sci. China* B **50** 494–500

[41] Nidhin M, Nazeer S S, Jayasree R S, Kiran M S, Nair B U and Sreeram K J 2013 Flower shaped assembly of cobalt ferrite nanoparticles: application as T_2 contrast agent in MRI *RSC Adv.* **3** 6906

[42] Murphy C J and Jana N R 2002 Controlling the aspect ratio of inorganic nanorods and nanowires *Adv. Mater.* **14** 80–2

[43] Salata O 2004 Applications of nanoparticles in biology and medicine *J. Nanobiotechnol.* **2** 3

[44] Longmire M, Choyke P L and Kobayashi H 2008 Clearance properties of nano-sized particles and molecules as imaging agents: considerations and caveats *Nanomedicine* **3** 703–17

[45] Faure A C, Dufort S, Josserand V, Perriat P, Coll J L, Roux S and Tillement O 2009 Control of the *in vivo* biodistribution of hybrid nanoparticles with different poly (ethylene glycol) coatings *Small* **5** 2565–75

[46] Tang Z, Zhao X, Zhao T, Wang H, Wang P, Wu F and Giesy J P 2016 Magnetic nanoparticles interaction with humic acid: in the presence of surfactants *Environ. Sci. Technol.* **50** 8640–8

[47] Zhang M, He X, Chen L and Zhang Y 2010 Preparation of IDA-Cu functionalized core–satellite Fe_3O_4/polydopamine/Au magnetic nanocomposites and their application for depletion of abundant protein in bovine blood *J. Mater. Chem.* **20** 10696

[48] Unsoy G, Yalcin S, Khodadust R, Gunduz G and Gunduz U 2012 Synthesis optimization and characterization of chitosancoated iron oxide nanoparticles produced for biomedical applications *J. Nanopart. Res.* **14** 964

[49] Wang Y X J, Hussain S M and Krestin G P 2001 Superparamagnetic iron oxide contrast agents: Physicochemical characteristics and applications in MR imaging *Eur. Radiol.* **11** 2319–31

[50] Thorek D L J, Chen A K, Czupryna J and Tsourkas A 2006 Superparamagnetic iron oxide nanoparticle probes for molecular imaging *Ann. Biomed. Eng.* **34** 23–38

[51] Wu W, Wu Z, Yu T, Jiang C and Kim W-S 2015 Recent progress on magnetic iron oxide nanoparticles: synthesis, surface functional strategies and biomedical applications *Sci. Technol. Adv. Mater.* **16** 23501

[52] Kin M, Kura H, Tanaka M, Hayashi Y, Hasaegawa J and Ogawa T 2015 Improvement of saturation magnetization of Fe nanoparticles by post-annealing in a hydrogen gas atmosphere *J. Appl. Phys.* **117** 17E714

[53] Wang B, Zhou M, Rozynek Z and Fossum J O 2009 Electrorheological properties of organically modified nanolayered laponite: influence of intercalation, adsorption and wettability *J. Mater. Chem.* **19** 1816

[54] Zhang J-M, Zhai S-R, Zhai B, An Q-D and Tian G 2012 Crucial factors affecting the physicochemical properties of sol–gel produced Fe_3O_4@ SiO_2–NH_2 core–shell nanomaterials *J. Sol-Gel Sci. Technol.* **64** 347–57

[55] Estelrich J, Sanchez-Martin M J and Busquets M A 2015 Nanoparticles in magnetic resonance imaging: from simple to dual contrast agents *Int. J. Nanomed.* **10** 1727–41

[56] Frias J C, Williams K J, Fisher E A and Fayad Z A 2004 Recombinant HDL-like nanoparticles: a specific contrast agent for MRI of atherosclerotic plaques *J. Am. Chem. Soc.* **126** 16316–7

[57] Hou Y, Yu J and Chu X 2016 *Advances in Nanotheranostics I* vol 6 ed Z Dai (Berling: Springer)

[58] Lam T, Avti P, Pouliot P, Maafi F, Tardif J-C, Rhéaume É, Lesage F and Kakkar A 2016 Fabricating water dispersible superparamagnetic iron oxide nanoparticles for biomedical applications through ligand exchange and direct conjugation *Nanomaterials* **6** 100

[59] Xiao L *et al* 2011 Water-soluble superparamagnetic magnetite nanoparticles with biocompatible coating for enhanced magnetic resonance imaging *ACS Nano* **5** 6315–24

[60] Chatterjee J, Haik Y and Chen C-J 2003 Size dependent magnetic properties of iron oxide nanoparticles *J. Magn. Magn. Mater.* **257** 113–8

[61] Li L, Jiang L-L, Zeng Y and Liu G 2013 Toxicity of superparamagnetic iron oxide nanoparticles: research strategies and implications for nanomedicine *Chin. Phys.* B **22** 127503

[62] Ahamed M, Alhadlaq H A, Khan M A M and Akhtar M J 2013 Selective killing of cancer cells by iron oxide nanoparticles mediated through reactive oxygen species via p53 pathway *J. Nanopart. Res.* **15** 1225